Hot-Electron Heating Caused by Two-Plasmon-Decay Instability

Introduction

High-energy electrons are detrimental to laser fusion because they can preheat the fuel, preventing the high compression necessary for central hot-spot ignition and high gain.[1] The direct-drive approach is particularly vulnerable as a result of the long scale length of plasma that exists at the quarter-critical density of the target, although it can also occur in indirect-drive geometry.[2]

Direct-drive–implosion experiments on OMEGA have observed hard x rays (a signature of hot electrons) that are coincident with the emission of half-integer harmonics and the predicted two-plasmon-decay (TPD) threshold.[3] Four-channel x-ray spectroscopy ranging in energies from 20 to 500 keV indicates hot-electron temperatures of $T_{hot} \lesssim 100$ keV for irradiation intensities of $I_0 \sim 10^{15}$ W/cm^2 at $\lambda_0 = 351$ nm (Ref. 4). Since electrons in excess of 100 keV are inferred experimentally via the hard x rays that they produce, it is apparent that the possibility of preheating exists. This will lead to an increased fuel adiabat and diminished fuel compressibility. Estimates of target preheat based on measured x rays are difficult, but likely fall in the range of 40 to 50 J, where the impact on target performance might be measurable on OMEGA (Delettrez *et al.* estimate a 40% reduction in areal density for a worst-case scenario on the basis of one-dimensional hydrodynamic calculations[5]).

Definitive evidence of preheat-impaired performance [e.g., in reduced areal density (ρR)] on OMEGA is currently lacking,[6,7] which complicates any extrapolation of preheat to ignition-scale designs. For example, in implosion experiments, close to 80% of maximum predicted areal density above 200 mg/cm^2 has been achieved using 10-μm-thick deuterated plastic (CD) ablators.[8] The TPD instability is only weakly excited in these targets. It can be more strongly excited by using thinner shells since the TPD threshold is more easily attained in hydrogenic plasma. While a significant degradation of ρR is observed for thinner CD ablators, it is not currently possible to rule out other competing mechanisms such as shock mistiming, hydrodynamic instability, radiation preheat, and preheat by nonlocal thermal electrons.

The need for a physical model of target preheat clearly exists. The self-consistent modeling, however, of hot-electron generation and the resulting preheating of the target is a very challenging problem. The purpose of this article is to present a model that represents an attempt in this direction. It includes aspects of the experimental conditions that are thought to be important. Namely, it assumes that all preheat is associated with TPD instability and the plasma inhomogeneities (density gradient) play an important role. The model contains nonlinearities that have been shown by detailed particle-in-cell calculations to play a dominant role in saturation.[9,10] The possibility of multiple acceleration stages for hot electrons as they periodically pass through the quarter-critical surface is also investigated. It takes the trajectory of the heated electrons that lies outside of the simulation boundaries into account. It is shown that, for the parameters of current OMEGA direct-drive cryogenic implosions, recirculation (or reheating) of electrons is an important effect.

While several simplifications are made, we attempt to show how, in future work, these simplifications may be systematically relaxed. The most important of these is the development of a self-consistent quasilinear model for the evolution of the electron distribution function[11] that would replace the current test-particle treatment.

The sections that follow describe the model for electron heating, with subsections describing the extended Zakharov model for the saturated electric field spectrum and outlining the test-particle method; present the results of electron-heating calculations; and, finally, present a summary and conclusions.

Description of a Model for Hot-Electron Production

Based on experimental observations, there are reasons to believe that TPD is the sole instability active in producing hot electrons in current OMEGA experiments. Half-integer harmonic signatures of TPD are strongly correlated with hard x-ray production, with x-ray energies of the order of $E_{x\ ray} \sim 100$ keV (Refs. 3 and 4). The onset of TPD signatures is also well predicted by the simple linear threshold for the absolute TPD

instability of a plane electromagnetic wave in a density gradient when the intensity of the plane wave is equated with the average overlapped-beam intensity on OMEGA. Thresholds for TPD in a linear gradient have been computed by a number of authors.[12–21] The "above-threshold parameter" $\eta = I_{14}L_{\mu m}/(320\,T_{\rm keV})$, which is based on the expression for absolute instability computed by Simon *et al*.,[13] $(v_{\rm osc}/v_{\rm e})^2 k_0 L > 4.134$ (i.e., the large β limit), has proven itself to be a very useful empirical tool for interpreting OMEGA experiments.[3,5,8] While the onset is well predicted by the η parameter, which signals absolute instability, the measured spectrum of plasma waves is generally not consistent with the absolutely unstable eigenmode.[3] Above threshold, the absolutely unstable wave corresponds to a forward-going plasmon of wave number close to k_0, where k_0 is the laser vacuum wave number, and a plasmon with small perpendicular wave number given by

$$k_\perp/k_0 = 0.02\, I_{14}^{1/4} (\lambda_0/0.351\,\mu m) \times (T_{\rm e}/2\,{\rm keV})^{-1} (L/150\,\mu m)^{-1/2},$$

while experimentally, most Langmuir wave (LW) intensity is found to be located close to the Landau cutoff ($k \sim 0.25\,k_{\rm De}$, where $k_{\rm De}$ is the Debye wave number).[3] This is not too surprising because convective growth can become important at similar intensities and can dominate the nonlinear state[9,22] because it is not as easily saturated as the absolute mode (see **Zakharov Model for the Saturated LW Spectrum**, below).

Raman backscattering is neglected in the model because of the absence of an experimentally observed Raman back-scattering signature. This is consistent with linear gain estimates: Raman scattering is expected to be convectively unstable below quarter-critical, with the Rosenbluth gain[23] $A_{\rm Ros} = \pi\gamma_0^2/|V_1 V_2 \kappa'|$ be-ing negligible for the relevant experimental parameters

$$A_{\rm Ros} \sim 0.04\, I_{14} (1 - n_{\rm e}/n_{\rm c})^{-1/2} (L_{\mu m}/150\,\mu m).$$

The envelope approximation, upon which the previous expression relies, is not valid near the quarter-critical density. Drake *et al*. have demonstrated the potential for absolute instability of stimulated Raman scattering (SRS) near the quarter-critical density[24] with the threshold condition

$$v_{\rm osc}/c > (1/2)(k_0 L)^{-2/3}.$$

The ratio of the TPD threshold to the above expression for absolute SRS is given approximately by

$$I_\nabla^{\rm 2P}/I_\nabla^{\rm R} = 0.9(T_{\rm e,keV}/2\,{\rm keV}) \times (0.351\,\mu m/\lambda_0)(L/150\,\mu m)^{1/3}.$$

It appears that the effects of absolute Raman scattering near the quarter-critical density should be taken into account. The model currently omits this possibility (and achieves a worth-while simplification by ignoring the equation for the envelope of the scattered transverse wave). This is based on the observations of the dominance of convective TPD over absolute TPD (see **Zakharov Model for the Saturated LW Spectrum**, below) and, by association, absolute Raman or high-frequency hybrid instability.[18,19] The neglect of these terms also appears consistent with results reported for explicit particle-in-cell (PIC) calculations.[9]

The spectrum of LW's driven by TPD instability is assumed to be saturated by nonlinearities that are contained within the extended Zakharov approximation.[25,26] Recent comparisons between the Zakharov model and reduced PIC calculations of TPD in homogeneous plasma indicate this to be a reasonable approximation.[10] The model takes into account the density gradients and flow velocities at quarter-critical that are predicted to occur experimentally on the basis of 1-D radiation–hydro-dynamic calculations using the *LILAC* code.[27]

Electron heating in response to this spectrum of electrostatic waves is computed in a test-particle approximation, i.e., the electron distribution is heated by the LW's, but the modified electron-distribution function does not act back on the LW's, i.e., there is no kinetic modification of the LW dispersion relation. This is done in order to make contact with experimental observations, as well as to investigate the effects of recirculating electron trajectories, which have for a long time been thought to be important.[11,28]

The test-particle approach to electron heating also allows for a systematic investigation of the validity of a self-consistent quasilinear model for TPD[11] along the lines of Sanbonmatsu *et al*.[29,30] by explicitly computing the diffusion of electron velocities, $\langle(\Delta \vec{v})^2/\Delta t\rangle$ (Refs. 31–33). This will be the subject of a future publication.

1. Zakharov Model for the Saturated LW Spectrum

The LW fields near the quarter-critical surface are modeled in the extended Zakharov approximation in two spatial dimensions taking into account a prescribed density gradient, as has been described previously,[25,26] and now extended here to include a prescribed flow velocity

$$\nabla \cdot \left[2i\omega_{p0}\left(\partial_t + \vec{v}_0 \cdot \nabla + \nu_e \circ \right) \right.$$
$$+ 3v_e^2 \nabla^2 - \omega_{p0}^2 \left(\delta n + \delta N\right) \Big] \vec{E}$$
$$= \left(e/4\,m_e\right) \nabla \cdot \left[\nabla \left(\vec{E}_0 \cdot \vec{E}^*\right) - \vec{E}_0 \nabla \cdot \vec{E}^* \right] + S_E. \quad (1)$$

In the above equation, $\vec{E}$ is the slowly varying complex envelope of the longitudinal electric field $\vec{\mathcal{E}}_l = 1/2\,\vec{E}\exp\left(i\omega_{p0}t\right) +$ c.c. (i.e., the electric field is decomposed into longitudinal and transverse components $\vec{\mathcal{E}} = \vec{\mathcal{E}}_l + \vec{\mathcal{E}}_t$. The quantity $\vec{E}_0$ is the slowly varying (in time) complex envelope of the transverse, electromagnetic (EM) field,

$$\vec{\mathcal{E}}_t = \sum_{j=1}^{N_j} \vec{E}_{0,j}\exp\left[i\vec{k}_{0,j}\cdot\vec{x} - i\left(\omega_0 - 2\omega_{p0}\right)t + i\phi_j \right],$$

which consists of N_j beams of amplitude $\vec{E}_{0,j}$ and of wave number $\vec{k}_{0,j}$ that differs only in direction $\left(\left|\vec{k}_{0,i}\right| = \left|\vec{k}_{0,j}\right|\right)$ and phase ϕ_j. The reference electron-plasma frequency is

$$\omega_{p0} = \left(4\pi n_0 e^2 / m_e\right)^{1/2},$$

and $v_e = \left(T_e/m_e\right)^{1/2}$ is the electron thermal velocity. For the slow density variation, $\delta n + \delta N$ represents the departure from the reference density $n_0 = 0.23\,n_c$, where $n_c = m_e\omega_0^2 / \left(4\pi e^2\right)$ is the laser critical density. The static, i.e., non-evolving, component of the electron density corresponds to a linearly increasing density profile,

$$N(x) \equiv n_0 + \delta N = \left[0.23 + 0.04\left(2x/l_x - 1\right)\right]n_c,$$

which varies from $0.19\,n_c$ to $0.27\,n_c$ over the simulation length l_x, where $x \in [0,l_x]$ and has a density scale length of $L_n^{-1} \equiv d\left[\log N(x)\right]/dx = (8/23)l_x^{-1}$. The value of L_n is assumed to be constant in time during the integration period of the Zakharov model. The evolving component $\delta n(\vec{x},t)$, a real quantity, satisfies the second Zakharov equation

$$\left[\left(\partial_t + \vec{v}_0 \cdot \nabla\right)^2 + 2\nu_i \circ \left(\partial_t + \vec{v}_0 \cdot \nabla\right) - c_s^2 \nabla^2\right]\delta n$$
$$= \frac{\nabla^2}{16\pi m_i}\left[\left|\vec{E}\right|^2 + \frac{1}{4}\left|\sum_j \vec{E}_{0,j}\exp i\left(\vec{k}_{0,j}\cdot\vec{x} + \phi_j\right)\right|^2\right] \quad (2)$$
$$+ S_{\delta n}, \quad (3)$$

which takes into account the ponderomotive force of the light waves, each having the phase ϕ_j. The low-frequency (LF) fluctuations are also driven by the ponderomotive pressure of the LW's, which is quadratic in $\vec{E}$. The damping operators $\nu_e \circ$

and $\nu_i \circ$ are local in k-space and contain the contribution of collisional and Landau-damping terms corresponding to a fixed Maxwellian ion- and electron-velocity distribution function of temperatures T_i and T_e, respectively. The terms S_E and $S_{\delta n}$ are noise terms that support a thermal level of LW and ion-acoustic-wave (IAW) fluctuations in the absence of other sources.[25]

The numerical domain $\Omega = [0,l_x] \times [0,l_y]$ on which the extended Zakharov model is solved is typically arranged so that the linear electron-density profile spans the range $0.19 < n_e/n_c < 0.27$. This ensures that the electric field associated with the LW's vanishes on the longitudinal boundaries. The electrostatic waves are damped at low density (large $k_{\lambda De}$) and reflected (turn) before encountering the boundary at the high-density side. Based on predicted scale lengths on OMEGA of $L_n \sim 150\,\mu$m, this translates into a spatial dimension l_x of approximately $l_x \sim 50\,\mu$m. The transverse dimensions are usually a few tens of microns. The transverse dimension should be as small as possible for computational efficiency, but no shorter than the correlation length for the LW fields. Typically, the transverse length l_y, where $y \in [0,l_y]$, is chosen to be $l_y \gtrsim 12.0\,\mu$m.

a. Zakharov predictions for the saturated LW spectrum. The nonlinear saturation of TPD based on the model presented in **Zakharov Model for Saturated LW Spectrum** (p. 67) is seen to involve a process of density-profile modification,[25,34] the generation of ion-acoustic-wave turbulence as a result of the ponderomotive response to primary TPD LW's,[9,25] LW cavitation and collapse, and Langmuir decay instability.[25] The development is quite similar to that observed in homogeneous reduced particle-in-cell calculations made recently by Vu et al.[10] and is broadly consistent with earlier observations that saturation occurs as a result of ion-wave fluctuations[35] or profile steepening.[34,36]

A series of two-dimensional calculations solving Eqs. (1) and (2) have been carried out with parameters motivated by conditions either currently or soon-to-be accessible on the OMEGA Laser System: the laser wavelength $\lambda_0 = 0.351\,\mu$m, the electron temperature $T_e = 2.0$ keV, the ion temperature $T_i = 1.0$ keV, ion charge $Z = 3.5$ (effective charge state corresponding to CH plasma), IAW damping of $\nu_{i0} \equiv \nu_i/kc_s = 0.1$, and density-gradient scale lengths in the range $L_n = (100$ to $350)\,\mu$m. The simulation domain was chosen so as to include densities from $n_e = (0.19$ to $0.27)\,n_c$. In the case of $L_n = 150\,\mu$m (which we define as the "canonical" scale length on OMEGA), $l_x = 45.0\,\mu$m, and $l_y = 12.0\,\mu$m (other cases were adjusted appropriately). The simulations were made with either a single-plane

electromagnetic (EM) wave ($N_j = 1$), normally incident along the direction of the density gradient ($\vec{k}_{0,1} \cdot \hat{e}_x / k_{0,1} = 1$), or with two overlapping plane waves ($N_j = 2$), each incident at an angle of $\theta_j = \cos^{-1}\left(\vec{k}_{0,j} \cdot \hat{e}_x / k_{0,j}\right) = \pm 0.23°$ to the direction of the density gradient (the calculations with two crossed beams allow for the sharing of a common plasma wave[10] that is thought to be an important experimental process on OMEGA.[37]) The plane of simulation is chosen to be coincident with the plane of polarization, which also assumes that all N_j beams are similarly polarized. The laser intensities I_L (incoherent overlapped "intensity" $I_L \equiv c/(8\pi)\sum_{i=1}^{N_j} \left|\vec{E}_{0,i}\right|^2$ in the case of multiple beams) were varied in the range $I_L = (5 \times 10^{14} - 2 \times 10^{15})$ W/cm². The combination of laser intensity and density scale length was chosen to put the absolute TPD instability in either the weakly unstable ($\eta \sim 1.5$) or moderately unstable regime ($\eta \sim 2$ to 3) with respect to the threshold criterion as defined by Simon *et al*.[13] Although there are differences between the single-beam and crossed-beam calculations, which will be described in a separate publication, the generic results described below are illustrative of both cases.

The calculations develop from the initial onset of absolute instability, which corresponds very well with the calculations of Simon *et al*.[13] with regard to both the threshold intensity and unstable wave number (eigenmode), toward a broad spectrum of plasmons as shown in Fig. 126.14(a). [The onset of absolute

instability and the resulting growth rate were determined accurately by removing the nonlinear coupling between the Eqs. (1) and (2). The threshold intensity was therefore observed to coincide with the Simon *et al*. prediction to within 10% for the normally incident single-beam case].

The absolutely growing mode eventually reaches a sufficient amplitude where nonlinearities become important. The time required for strong nonlinearity to become important for canonical OMEGA parameters based on an initial noise level of $\left\langle \left|E\right|^2 \right\rangle / (8\pi n_0 T_e) = 6 \times 10^{-6}$ and a laser intensity of $I_L = 10^{15}$ W/cm² was found to be ~ 1.2 ps. Density-profile modification[34] was the saturating mechanism of the absolute modes in these calculations. This was determined by performing an estimate of the local steepening of the density gradient by taking a transverse (y direction) average of the density $\tilde{N}(x) \equiv \left\langle N(x) + \delta n(x,y) \right\rangle_y$ (as shown in Fig. 126.15) and estimating the modified gradient scale length in the neighborhood of the quarter-critical density $L_{\mu m}$. The observed scale length, when substituted into the threshold expression, was found to lead to marginal stability $\eta = I_{14}\tilde{L}_{\mu m}/(230\,T_{keV}) \sim 1$. This situation was found to hold for all calculations that were performed. The collapse in growth of the initially unstable eigenmode is followed by an expanding region of large LW excitation at lower densities (corresponding to larger $k_\perp$ LW's in the single-beam case). This is seen in the Fourier spectrum
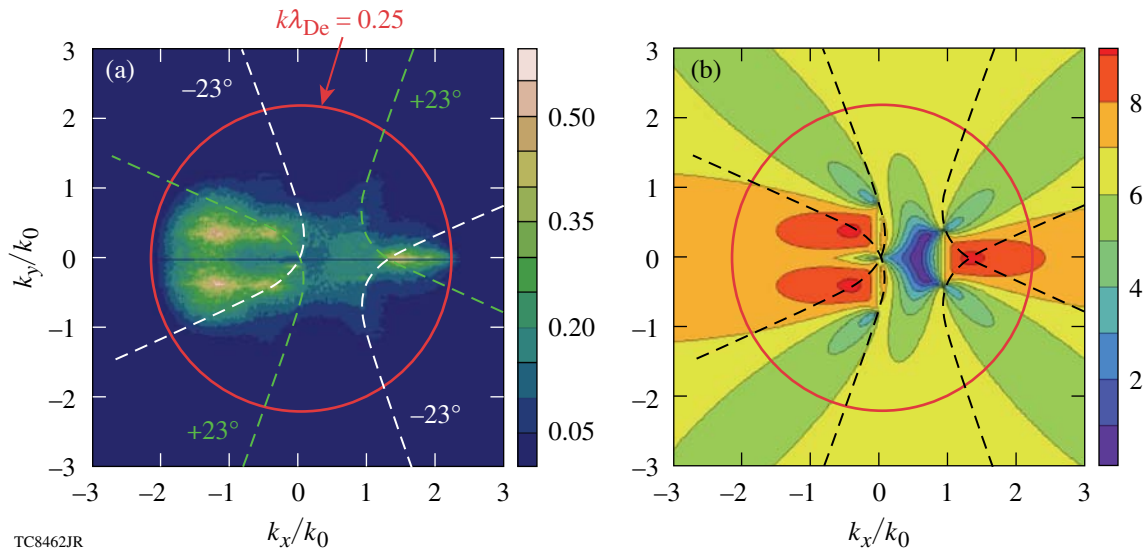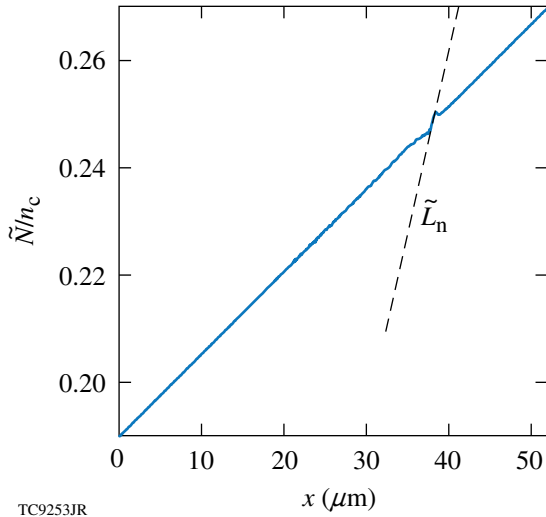

Figure 126.14
(a) The saturated Langmuir wave spectrum in Fourier space $\left|\vec{E}_k\right|^2$ corresponding to a crossed-beam irradiation geometry with an overlapped intensity of $I_L = 1 \times 10^{15}$ W/cm² (canonical OMEGA parameters). Two EM waves are incident at angles of $\pm 23°$. For each beam, the single-beam maximum-growth-rate curves for TPD[10] are shown as dashed lines, while the solid red line defines the Landau cutoff. (b) The TPD growth rate in arbitrary units from the theory of Short[37] for the same parameters as in (a).

Figure 126.15
The solid line shows the modified 1-D density profile $\tilde{N}(x) \equiv \langle N(x) + \delta n(x,y) \rangle_y$ normalized to the critical density n_c, taken at the time of saturation of the absolutely unstable eigenmode ($t = 1.2$ ps) for the simulations described in **Zakharov Predictions for the Saturated LW Spectrum** (p. 68). The dashed line approximates the slope in the neighborhood of quarter critical and is used to define the modified density scale length $\tilde{L}_n$.

of the longitudinal electric-field intensity [Fig. 126.14(a)], where the active region of LW's extends as far as the Landau cutoff at wave numbers $k \sim 0.25\ k_{De}$ (solid red line). These unstable modes, which are convective in nature, come to dominate the saturated LW spectrum at later times. The broad spectrum in Fig. 126.14(a), which corresponds to irradiation by two crossed beams, is dominated by the common LW and its associated daughter waves. This can be seen by comparing the spectral features in Fig. 126.14(a) with the expected growth rate based on a multiple-beam theory for identical parameters[37] [Fig. 126.14(b)]. The predicted maximum growth rate occurs at the intersection of the single-beam maximum growth rate curves (shown by the dashed lines) in Fig. 126.14. The growth rate has quite a broad peak, extending beyond the Landau cutoff (solid circle) for positive wave numbers—although the crossed-beam theory ignores wave damping. The absolute mode would appear to be relatively unimportant in the saturated state.

Yan et al.[9,22] demonstrated that the convective Rosenbluth gain in amplitude [$g_R \sim \exp(\pi\Lambda)$] for the large $k_\perp$ TPD modes can be simply written in terms of the Simon et al. threshold parameter for absolute instability

$$\pi\Lambda = 2.5\left(1 - 0.0088\, T_{keV} - 0.0047\, T_{keV}\, \tilde{k}_\perp^2\right)\eta,$$

where $\tilde{k} \equiv ck/\omega_0$. Convective gain in intensity is therefore several times larger than the threshold parameter and very weakly

dependent upon the transverse wave number for the parameters of current interest. Close to threshold, all transverse modes up to the Landau cutoff can saturate convectively without the need for nonlinear processes. As laser intensity increases, these convective modes are observed to saturate as a result of the excitation of large-amplitude ion-acoustic perturbations with relative-density perturbations on the few-percent level.

Features of the growth and nonlinear saturation of Fourier modes that come to dominate the spectrum at times $t \gtrsim 1.2$ ps in the case of single-beam illumination are illustrated in Fig. 126.16. The left-hand column [Figs. 126.16(a)–126.16(c)] shows a series of snapshots of the low-frequency density perturbations $\langle \delta n \rangle_{rms}(x)/n_c$ taken at different times (see figure caption). Note that the reference n_0 and linearly varying part of the density $\delta N(x)$ have been extracted and that a one-dimensional lineout has been obtained by taking the root-mean-square (rms) average over the transverse (y) coordinate,
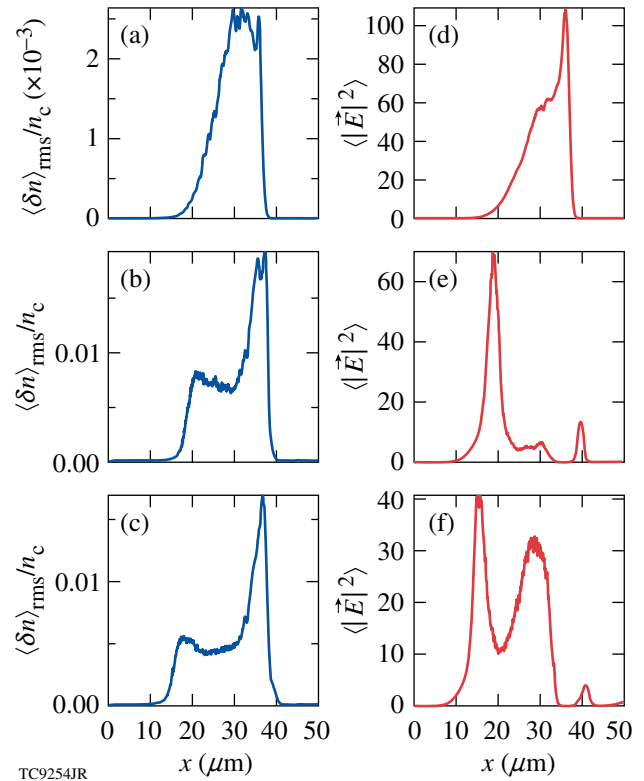
Figure 126.16
The left-hand column [(a)–(c)] shows a series of snapshots of the 1-D density perturbation $\langle \delta n \rangle_{rms}/n_c$, while the right-hand column [(d)–(f)] shows the transverse average of the LW excitation level $\langle |\vec{E}|^2 \rangle$, both plotted against the longitudinal coordinate x (in microns). From top to bottom, the rows correspond to times $t = 1.2$, $t = 2.0$, and $t = 2.4$ ps. The figure illustrates the correlation between LW amplitude and the region over which $\langle \delta n \rangle_{rms}/n_c \gtrsim 0.5\%$.

$$\langle \delta n \rangle_{\mathrm{rms}}(x_i) \equiv \left[(1/n_y) \sum_{j=1}^{n_y} \delta n (x_i, x_j)^2 \right]^{1/2},$$

where n_y is the number of transverse grid points. The right-hand column [Figs. 126.16(d)–126.16(f)] shows the normalized LW excitation level $\langle |\vec{E}|^2 \rangle$ averaged over the transverse direction.

Figure 126.16(a) shows the situation at $t = 1.2$ ps, where the convective LW growth is well described by the linear evolution. The excitation of the LF density perturbations is due to the non-linear ponderomotive force [first term on the left side of Eq. (2)] of the unstable LW's and has a negligible effect on LW growth given by Eq. (1) (its contribution is negligible compared to the damping rate, for example). In Fig. 126.16(d), the LW's appear to grow more rapidly at higher density for reasons that are not fully understood. As time progresses [Fig. 126.16(b)], the density perturbation $\langle \delta n \rangle_{\mathrm{rms}}(x)$ level has grown significantly and is at the few-percent level. A two-dimensional Fourier analysis of the density perturbations (not shown) reveals these perturbations to be IAW's driven in response to the pondero-motive beating of primary TPD LW's, a feature previously identified in the reduced PIC calculations of Vu et al.[10] The absolute mode has saturated as described above. Notice that the maximum in the LW excitation level $\max \left[\langle |E|^2 \rangle (x) \right]$ occurs at roughly $x = 19$ μm, which is the point where $\langle \delta n \rangle_{\mathrm{rms}}(x)/n_c$ falls below 0.5%. This peak in LW excitation moved to this location continuously from near $n_e = 0.25\ n_c$, following the boundary of density excitations. For larger values of x, there is evidence of saturation of the LW amplitude. The saturation leads to a lower level of LW amplitudes and a weakening of the ponderomotive excitation of δn.

The onset of a new type of behavior is shown in Figs. 126.16(c)–126.16(f). The LF density perturbations have decreased to a value of $\langle \delta n \rangle_{\mathrm{rms}}/n_c \lesssim 0.5\%$. This appears to permit some renewed growth of the LW's (i.e., at $x = 30$ μm) and leads to a new peak in LW excitation located close to the minimum in $\langle \delta n \rangle_{\mathrm{rms}}/n_c$. This close correlation between the evolution of $|E|^2$ and δn is given as evidence of the detuning effect of LF density perturbations on the convective growth of TPD modes. We recall that this is the same mechanism proposed as the saturation mechanism for TPD in the *OSIRIS* PIC calculations of Yan et al.[9] It would appear that density perturbations need to exceed the level $\langle \delta n \rangle_{\mathrm{rms}}/n_c \approx 0.5\%$ in order to be effective. An alternate description of nonlinear saturation will be given in a paper by Vu et al.,[38] where evidence is presented from RPIC and Zakharov simulations that Langmuir collapse is the essential dissipative saturation mechanism in these relatively weakly driven regimes, with the Langmuir decay instability (LDI) playing a minor role.

In general, the evolution of the LW spectrum to a steady state is observed to take several tens of picoseconds. While oscillations of the kind described above persist, the spectrum becomes "steady" only after roughly one acoustic transit time across the density range Δn spanning from the Landau cutoff to quarter-critical. For canonical parameters, this time is $t_{\mathrm{sat}} \sim \Delta x / c_s = (\Delta n / n_0)\ L_n \times 1/c_s \approx 100$ ps. This steady LW spectrum is used below to investigate the generation of hot electrons.

b. Estimate of the maximum energy gain for an electron in transit through the interaction region. The late-time (saturated) LW spectrum obtained from the Zakharov calculations on p. 68, although broad, is dominated by a shared common wave and the corresponding daughter waves whenever the irradiation consists of symmetrically arranged, overlapping plane waves (Fig. 126.14) (an effect that may explain the experimentally observed scaling of preheat on overlapped-beam intensities[4]). Since this is the usual experimental configuration on OMEGA, consider the simple case where the action on the plasma electrons is due to a single coherent LW wave. In this case, an estimate for the expected scale of electron heating can be obtained (although it should be noted that similar numbers can be obtained without invoking the common wave). Taking the wave numbers of the LW's at their point of origin to be $k\lambda_{\mathrm{De}} = 0.16$ and 0.07, respectively (see Fig. 126.14) (the common wave is only resonant at a particular density;[10] here the density is $n_e / n_c = 0.241$), then the trapping width can be estimated from the formula

$$v_{\mathrm{tr}} = 2 \left(e \mathcal{E}_l / m_e k \right)^{1/2} = 2 \left(v_{\mathrm{osc}} v_\phi \right)^{1/2},$$

where $v_{\mathrm{osc}} = e \mathcal{E}_l / (m_e \omega)$ is the oscillatory velocity of an untrapped electron and $v_\phi / v_{\mathrm{Te}} = 1/k\lambda_{\mathrm{De}} \left(1 + 3k^2 \lambda_{\mathrm{De}}^2 \right)^{1/2}$ is the LW phase velocity for a wave satisfying the Bohm–Gross dispersion relation $\omega^2 = \omega_p^2 \left(1 + 3k^2 \lambda_{\mathrm{De}}^2 \right)$. In practical units the trapping width becomes

$$\frac{v_{\mathrm{tr}}}{v_{\mathrm{Te}}} = 0.37 \left(\frac{1}{k\lambda_{\mathrm{De}}} \right)^{1/2} \left(\frac{\lambda_0}{0.351\ \mu\mathrm{m}} \right)^{1/2}$$

$$\times \left(\frac{I_{14}}{T_{e,\mathrm{keV}}} \right)^{1/4} \left(\frac{\mathcal{E}_l}{\mathcal{E}_t} \right)^{1/2}. \tag{4}$$

Substituting the wave numbers for the common and daughter waves gives the values

$$v_{\mathrm{tr}} = 1.38\ v_{\mathrm{Te}} \left(\mathcal{E}_l / \mathcal{E}_t \right)^{1/2}$$

and $2.1\ v_{\mathrm{Te}} \left(\mathcal{E}_l / \mathcal{E}_t \right)^{1/2}$, respectively. In both cases the trapping width is insufficient to trap thermal electrons because of the

high phase velocity of the waves (v_ϕ/v_{Te} = 6.49 and 14.40 for the common and daughter LW's, respectively). As a result, wave breaking will not easily occur.[39]

The presence of the density gradient modifies the propagation of the TPD-produced LW's from their point of origin. Theoretical treatments of wave–particle interaction that lead to particle trapping and acceleration most often consider unbounded homogeneous plasma.[40,41] The present situation involves both a spatially localized region of LW excitation (excitation is restricted to densities in the range $0.2 \lesssim n_e/n_c \lesssim 0.25$) and plasma inhomogeneity. Of most importance is the inhomogeneity in the plasma density. For example, the common wave, which is blue shifted with respect to $\omega_0/2$, propagates up the density gradient. For a freely propagating LW of fixed frequency ω, the wave number will decrease in order to preserve the dispersion relation as the local density (and plasma frequency) increases. The phase velocity will likewise increase $v_\phi = v_{Te}\left\{3\omega^2/\left[\omega^2 - \omega_p(x)^2\right]\right\}^{1/2}$, at some point becoming superluminal (the group velocity has the opposite dependence, $V_g = 3v_{Te}/v_\phi$). The density at which the LW will turn depends on its frequency. The daughter wave (red-shifted plasmon) propagates down the gradient. Its phase velocity decreases until it becomes a few times the thermal velocity and the wave is damped (the Landau cutoff).

The density gradient creates the potential for electron acceleration to higher energies than can be obtained in homogeneous plasma since the phase-velocity increase can keep pace with the electron as it is accelerated up the gradient.[42] Given an arbitrary LW amplitude, it might be possible to accelerate electrons to arbitrarily high energies, but, practically, there will come a point at which the maximum acceleration in the LW field will be insufficient to match the acceleration of the LW phase velocity. Following Brooks et al.[42] (with a trivial generalization to include relativistic velocities), the magnitude of the largest-attainable acceleration may be simply obtained from the relativistic momentum equation for electrons $|v'|_{max} = e\mathcal{E}_l/\left(\gamma^3 m_e\right)$ by assuming the electron maintains constant phase with respect to the LW. In practical units the maximum-attainable acceleration is

$$\left|v'_{ph}\right|_{max} = 1.5 \times 10^{24}\, I_{15}^{1/2}\, \gamma^{-3}\left(\mathcal{E}_l/\mathcal{E}_t\right)\ \text{cm/s}^2,$$

where the prime denotes the time derivative. Equating this with the acceleration of the LW phase velocity up the density gradient $v'_\phi(x) = v_\phi^2(x)\omega_p(x)^2\left[\omega^2 - \omega_p^2(x)\right]^{-1}/(2L_n)$ enables one to calculate the location x and phase velocity at which the electron can no longer remain in phase $(v_\phi)_{max}$—the above is solved iteratively since the relativistic gamma factor is dependent on the phase velocity $\gamma(v_\phi) = \left(1 - v_\phi^2/c^2\right)^{-1/2}$.

The energy gain is given by $\Delta E/(m_e c^2) = \gamma\left[(v_\phi)_{max}\right] - \gamma\left[(v_\phi)_0\right]$, where $(v_\phi)_0$ is the initial (phase) velocity of the electron (LW). Substituting in values $I_{15} = 1$, $\mathcal{E}_l = \mathcal{E}_t$, and $(v_\phi)_0 = 6.49\, v_{Te}$ from the Zakharov calculations presented in **Zakharov Predictions for the Saturated LW Spectrum** (p. 68) gives an estimate for the energy gain of $\Delta E \sim 110$ keV (or $\Delta E \sim 177$ keV for $\mathcal{E}_l = 2\, \mathcal{E}_t$).

The actual situation does not involve a single coherent wave, but rather there are many waves whose resonances are expected to have significant overlap, leading to orbits that become diffusive. It might be possible to approximate the stochastic acceleration of electrons in the predicted LW fields with a self-consistent Fokker–Planck[43] or quasilinear model.[11,29,30] To estimate the heating effect more accurately and to investigate the importance of reheating, test electron trajectories are directly integrated in the LW fields predicted by the Zakharov model of **Zakharov Predictions for the Saturated LW Spectrum** (p. 68). This will also form the basis for future work that will examine the applicability of quasilinear diffusion[32–44] for the two-plasmon-decay instability.

2. Test-Particle Equations of Motion

Test-particle motion is governed by the relativistic Newton–Lorentz equations. For the ith electron test particle, these are

$$\frac{d\vec{x}_i}{dt} = \vec{v}_i, \tag{5}$$

$$\frac{d\vec{p}_i}{dt} = -e\left[\vec{\mathcal{E}}_l(\vec{x}_i, t) + \vec{\mathcal{E}}_t(\vec{x}_i, t) + \vec{v}_i/c \times \vec{\mathcal{B}}(\vec{x}_i, t)\right], \tag{6}$$

where $\vec{p}_i = \gamma_i m_0 \vec{v}_i$ is the electron momentum. The longitudinal electric field $\vec{\mathcal{E}}_l$ is associated with the LW's resulting from the TPD instability and is obtained from the Zakharov field $\vec{E}$ by restoring the carrier frequency ω_{p0} (which was explicitly removed in the Zakharov approximation)

$$\vec{\mathcal{E}}_l(\vec{x}, t) = 1/2\, \vec{E}(\vec{x}, t)\exp\left(-\omega_{p0} t\right) + \text{c.c.} \tag{7}$$

The transverse fields $\vec{\mathcal{E}}_t$ and $\vec{\mathcal{B}}$ are associated with the incident laser light and are currently ignored when computing test-particle trajectories (they are prescribed fields in the current extended Zakharov model). Although the transverse electric-field strength is quite large,

$$\mathcal{E}_t \sim 8.7 \times 10^8 \left(I_0/1 \times 10^{15}\ \text{W/cm}^2\right)^{1/2}\ \text{V/cm},$$

it is not effective in accelerating electrons at nonrelativistic laser intensities ($I_0 \lesssim 10^{18}$ W/cm^2). The transverse fields result merely in a "quiver" imposed on the unperturbed motion. The

quantity $\vec{\mathcal{E}}_l$ is defined only at discrete spatial locations that are determined by the discretization (grid points) used in the numerical solution of Eqs. (1) and (2) and is interpolated onto the ith test electron position $\vec{x}_i$ using bilinear interpolation. The test-particle equations [Eqs. (5) and (6)] are integrated numerically using a fourth-order Runge–Kutta scheme.

Ensemble averages of test-particle quantities are obtained by averaging over test-particle initial conditions $\vec{x}_i(t = 0)$ and $\vec{p}_i(t = 0)$ since averaging over realizations of the electric-field spectrum is impractical. The initial position of a test particle $\vec{x}_0 \equiv \vec{x}(t = 0)$ is a random variable defined on $\Omega = [0, l_x] \times [0, l_y]$ with a uniform probability distribution $f(\vec{x}_0)d\vec{x}_0 = d\vec{x}_0/(l_x l_y)$. The initial momentum $\vec{p}_0 \equiv \vec{p}(t = 0)$ is given by

$$\vec{p}_0 = p_0\left[\hat{e}_x \sin(\phi) + \hat{e}_y \cos(\phi)\right],$$

where the magnitude of the momentum p_0 is fixed according to a given kinetic energy

$$p_0 = m_0 c\left[\left(T_0 \big/ m_0 c^2 + 1\right)^2 - 1\right]^{1/2},$$

while the angle ϕ is a uniform random variable on $[0, 2\pi]$ with the probability distribution $f(\phi)d\phi = d\phi/(2\pi)$. The effect of the finite boundary on the particle trajectories is addressed in the following section, while the boundary conditions on the longitudinal fields are periodic in the transverse direction $\vec{\mathcal{E}}_l(x, y + l_y) = \vec{\mathcal{E}}_l(x, y)$ and vanish at the longitudinal boundaries $\vec{\mathcal{E}}_l(x = 0, y) = \vec{\mathcal{E}}_l(x = l_x, y) = 0$ (see Fig. 126.17).

3. Estimation of Global Particle Trajectories

For the numerical simulation of Eqs. (5) and (6), any potential for electrons to re-enter the TPD active region after their transit through the simulation domain must be manifested through the boundary conditions because of limitations placed on the maximum size of the region over which Eqs. (5) and (6) can be realistically integrated. In general, the problem of boundary conditions in kinetic[29,30] or PIC calculations[9] is usually addressed by assuming that transverse boundaries are periodic, while longitudinal boundaries are thermalizing. The thermal boundary conditions have the effect of driving the electron-distribution function to a Maxwellian,[30] which may or may not be physically reasonable. It is clear that the choice of boundary condition has a significant impact on the properties of the hot-electron spectrum.[11,28] Such a "thermalizing" scheme is easily implemented for test particles in Eqs. (5) and (6) above. Inspection of the target areal densities relevant to OMEGA implosions at the time of TPD instability ($\rho R \sim 10^{-2}$ g/cm^2) shows, however, that they are unlikely to be completely stopped [the range $r_0 = 6.65 \times 10^{-2}$ g/cm^2 for an electron of energy of 100 keV in hydrogen in the continuous-slowing-down approximation—energies corresponding to those estimated in **Estimate of the Maximum Energy Gain for an Electron in Transit Through the Interaction Region** (p. 71) and observed experimentally[4]].[45] As a result, an estimate of the effect of electron recirculation is needed.

The spherical nature of the quarter-critical surface means that hot electrons can pass through the center of the target and re-encounter it once more on the opposite side (as long as they are sufficiently energetic so as not to range out; i.e., trajectories of type A, shown in Fig. 126.18). Less obvious is the fact that electrons on outward-bound trajectories (heading away from the target) may also be reflected back by the presence of sheath fields[11,46,47] (trajectory of type B, shown in Fig. 126.18). The possibility therefore exists for complex orbits where electrons can be accelerated multiple times by the TPD active region near the quarter-critical surface.
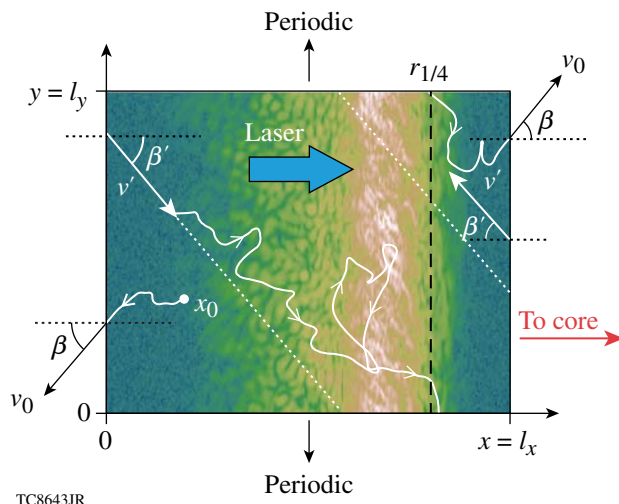

Figure 126.17
An illustration of how the boundary conditions for electron test particles are implemented. The region $\Omega = [0, l_x] \times [0, l_y]$ over which the LW fields are calculated is shown, where the colors correspond to the magnitude $\left|\vec{E}(x, y)\right|^2$ from a particular run. Periodicity is assumed for trajectories crossing the transverse boundaries ($y = 0$ or $y = l_y$), while a test particle reaching a longitudinal boundary ($x = 0$ or $x = l_x$) at time t with angle β and energy E_0 is re-injected at the same boundary at the later time $t' = t + \Delta t$ with a reduced energy $E' = E_0 - \Delta E$. The position along the boundary at reinjection is randomized, while its angle is given by $\beta' = \beta$. The white curve illustrates this process for an imaginary trajectory.
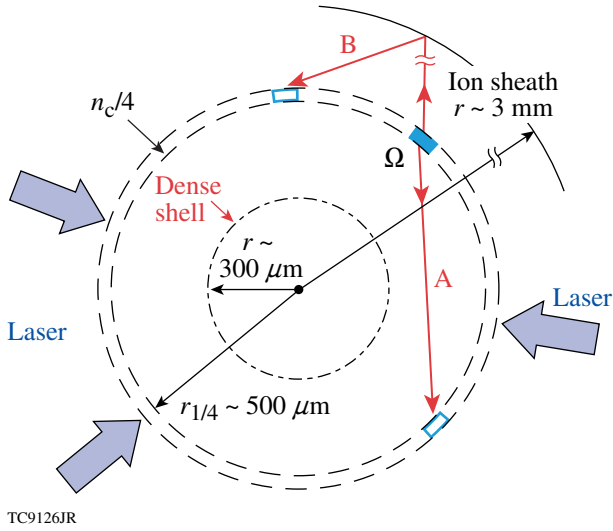
TC8643JR

TC9126JR

Figure 126.18
A schematic drawing showing a two-dimensional plane passing through the origin of a spherical implosion and containing the plane region Ω over which the extended Zakharov equations are simulated. The region Ω is illustrated by the blue shaded rectangle spanning the radius of the quarter-critical density surface, $r_{1/4}$. Periodicity (modulo l_y) is assumed in the tangential direction so that the whole annular region bounded by the dashed concentric circles is assumed to be modeled (mapped onto) Ω. Because of the spherical geometry, electrons that leave the region Ω in the direction of the origin (trajectory of type A as indicated) can re-intersect the quarter-critical surface and re-enter Ω. Outgoing trajectories (type B) can also return because of reflection from the ion sheath. Dimensions characteristic of OMEGA implosions are indicated.

The global radiation hydrodynamics of an imploding target at any given time during an implosion is calculated with the one-dimensional radiation–hydrodynamics code *LILAC*[27] without consideration of the effects of TPD (i.e., no increased absorption or effects of preheat). The parameters are taken to be those of current cryogenic implosion experiments on OMEGA at the time of peak TPD instability. These parameters place the quarter-critical surface at a radius of $r_{1/4} \sim 500~\mu m$, while the dense shell is at a radius of approximately 300 μm (see Fig. 126.18). The energy loss and time of flight associated with the electron trajectories beyond the quarter-critical surface are approximated below by "unperturbed" trajectories. That is, the energy loss and time of flight between an electron leaving the critical surface and returning (either by passing through the core or by reflection by sheath fields far out in the corona[46]) are estimated assuming a straight-line trajectory with angle and energy given by the values on leaving the quarter-critical surface. The time of return will be delayed by an amount that is dependent on the particular boundary that has been crossed and the details of the trajectory. Periodicity in the transverse (y) direction is motivated by the fact that the radius of curvature of the quarter-critical surface is much larger (typically ten times

larger) than the lateral extent l_y of the simulation volume (and therefore the correlation length for $\vec{E}$).

a. Practical implementation of delay-type boundary conditions on test particles. At the boundary of the Zakharov calculation located at $x = l_x$ (see Fig. 126.17), which looks toward the target core, electrons crossing at time t with angle $\beta = \cos^{-1}(\vec{p} \cdot \hat{n}/p)$ with respect to the outward normal $\hat{n}$ of the simulation volume $(\hat{n} = \hat{e}_x)$ cut a chord of length $s_{max} = 2~r_{1/4}\cos(\beta)$ across the circle that describes the intersection of the quarter-critical surface with the plane defined by the laser polarization vector and the radius vector defined with respect to target origin (Fig. 126.18). Note that this angle (β) is, to an excellent approximation, the same as the angle between the negative radius vector and the electron momentum vector $(\hat{n} \approx -\hat{e}_r)$. The radius $r(s)$ along this chord as a function of path length s is given by $r^2 = r_{1/4}^2 + s^2 - 2(r_{1/4}s)\cos(\beta)$, and inverting this function allows one to specify the hydrodynamic variables $n_e(r)$, $T_e(r)$ from the hydrocode *LILAC* along the trajectory, $n_e(s)$, $T_e(s)$. The time of flight for an electron to transit the path is estimated by

$$\Delta\tau = \frac{1}{c}\int_0^{s_{max}} \frac{ds}{\beta_e(s)}, \tag{8}$$

where the particle velocity is computed in terms of its energy $E(s)$ according to

$$\beta_e(s) = \left\{ \frac{2E(s)/m_e c^2 + \left[E(s)/m_e c^2\right]^2}{\left[1 + E(s)/m_e c^2\right]^2} \right\}^{1/2} \tag{9}$$

with

$$E(s) = E_0 - \int_0^s \left|\frac{dE}{ds}\right| ds \tag{10}$$

being the kinetic energy of the electron as a function of distance s along the path. The total energy loss along the path is simply $\Delta E = E_0 - E(s_{max})$. The stopping power $-dE/ds$ is given by $-dE/ds = e^2 \omega_p^2/(c^2\beta_e^2)\log\left[\beta_e^2 m_e c^2/(\hbar~\omega_p)\right]$. With the above assumptions, the energy loss ΔE and time delay Δt may be computed as a function of energy E_0 and angle β.

As mentioned previously, there is also a possibility that electrons leaving the outer simulation boundary ($x = 0$) (see Fig. 126.17) will return. This time, the effect is not geometrical but is instead related to the formation of a plasma sheath far out in the corona[46,47] (see Fig. 126.18). In principle the structure and dynamics of the sheath formation are complicated and coupled to the hot-electron–generation mechanism itself, which

requires a level of knowledge that is currently unavailable. Here we take a practical approach and adopt a greatly simplified model that has been previously used by Delettrez *et al*.[5] This has the advantage of facilitating comparisons between the current work and the phenomenological model of Delettrez *et al*. The model specularly reflects electrons when they reach the radius of the last Lagrangian cell of the *LILAC* calculation. The total path length is therefore given by $s_{max} = 2\,l_{exc}$, where $l_{exc} = r_{sh}\cos(\Theta) - r_{1/4}\cos(\beta)$ is the distance to the last Lagrangian cell of the *LILAC* calculation, r_{sh} is its radius, and $\Theta = \sin^{-1}\left[r_{1/4}/r_{sh}\sin(\beta)\right]$. The radius is now given in terms of the path length according to $r^2 + s^2 + r_{1/4}^2 + 2\left(r_{1/4}s\right)\cos(\beta)$ for $s \le l_{exc}$, and by $r^2 = \left(2l_{exc} - s\right)^2 + r_{1/4}^2 + 2r_{1/4}\left(2l_{exc} - s\right)\cos\beta$ for $s > l_{exc}$.

The energy losses and time delays as a function of electron momentum (energy and angle) are precomputed and stored in look-up tables, one for each longitudinal boundary. Figures 126.19 and 126.20 show examples of look-up tables for the boundary at $x = l_x$ corresponding to a cryogenic implosion on OMEGA (shot 45009) at the time of experimental onset of two-plasmon-decay signatures (roughly 2.5 ns from the start

of the pulse). Test particles, upon reaching the boundary, are re-injected at the same boundary at a later time $t + \Delta t$ with the modified angle $\beta' = -\beta$ and energy $E_0 - \Delta E$. The transverse coordinate of the returning electron is randomized, taking the new position to be a uniform random variable on $[0, l_y]$. This is illustrated in Fig. 126.17. If a particular energy loss results in a re-injected energy of the electron falling below a threshold value (typically $E_{cut} = 200$ eV), the trajectory is terminated.

TC8646bJR
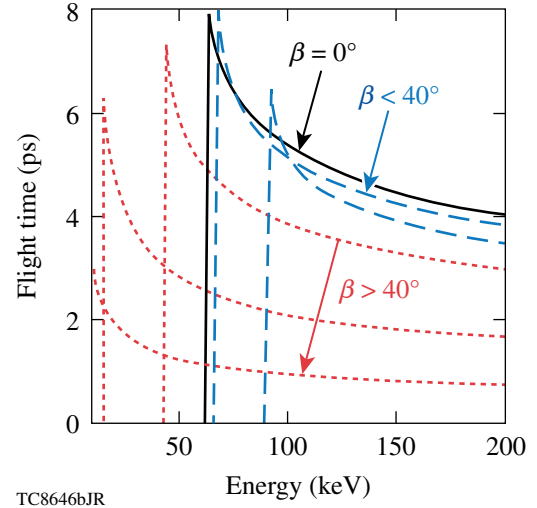
Figure 126.20
An example of the boundary look-up tables for time delay Δt at the $x = l_x$ simulation boundary corresponding to OMEGA shot 45009 at time $t = 2.5$ ps. The delay reaches a maximum value of $\Delta t \sim 8$ ps for trajectories that are nearly radial (inward) ($\beta \approx 0°$), and it vanishes for tangential trajectories $\beta = 90°$. The curves types/colors are the same as described in Fig. 126.19.

Results of Test-Particle Calculations

To quantify the contributions from separate processes, the effect of heating is first calculated with absorbing/thermal boundary conditions in the longitudinal direction, while periodicity is assumed in the transverse direction. This corresponds either to a massive target in which all hot electrons range out or alternatively to the usual boundary conditions that are applied in the kinetic modeling of TPD using PIC codes.[9,10] The density scale length is varied within the range $L_n = (100$ to $350)$ μm, while holding the electron temperature fixed at $T_e = 2$ keV. This addresses the range currently accessible on OMEGA and, for the longer scale lengths, the range accessible in the near future on OMEGA EP. The laser intensities are chosen to be between $I_L = (0.1$ to $2.0) \times 10^{15}$ W/cm^2. With this choice, the absolute TPD instability is found to be slightly above threshold to approximately three times above threshold [$\beta = (1.15$ to $3.1)$] according to the formula of Simon *et al*.[13] Finally, the impact of reheating is addressed by taking as an example the hydro-
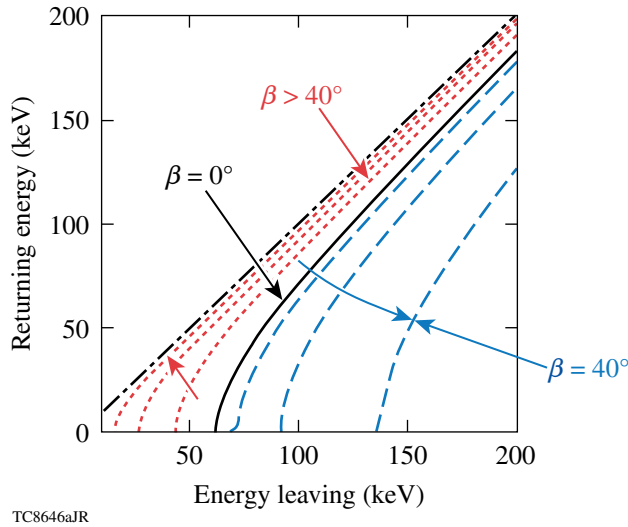

TC8646aJR

Figure 126.19
Look-up tables for energy loss at the $x = l_x$ boundary (i.e., type-A trajectories in Fig. 126.18) corresponding to OMEGA shot 45009 at time $t = 2.5$ ns. Angle β is the angle between the outward normal of the boundary $\left(\approx -\hat{e}_r\right)$ and the direction of the electron-velocity vector (see Fig. 126.17). As β increases from 0° [radially inward trajectory (black solid curve)] to $\beta \lesssim 40°$, the energy loss increases (i.e., the blue dashed curves move as indicated by the arrow). The effect is due to the increased path length in the dense compressed shell (see Fig. 126.18). Maximum energy loss occurs at $\beta \approx 40°$. For angles greater than 40° (red dotted curves) the energy loss falls dramatically and vanishes at $\beta = 0°$ since the trajectories no longer intersect the dense shell and the path length vanishes.

dynamic conditions of a cryogenic implosion that has been fielded on OMEGA (shot 45009) and computing the effects of reheating on the hot-electron temperature as the laser intensity is increased (within the above quoted range).

Figure 126.21 shows the energy distribution of test electrons as a function of electron energy for a typical case. The initial energies were chosen from a Maxwellian distribution of temperature $T_e = 2$ keV, chosen to be consistent with the electron temperature used in the Zakharov calculation. Note that the deviation from the initial Maxwellian occurs at an electron kinetic energy of roughly 20 keV. This is consistent with the smallest phase-velocity waves (largest wave number) observed in the LW spectrum (Fig. 126.14). The tail is well fit by an exponential, the slope of which is used to define an effective hot-electron temperature T_{hot}.
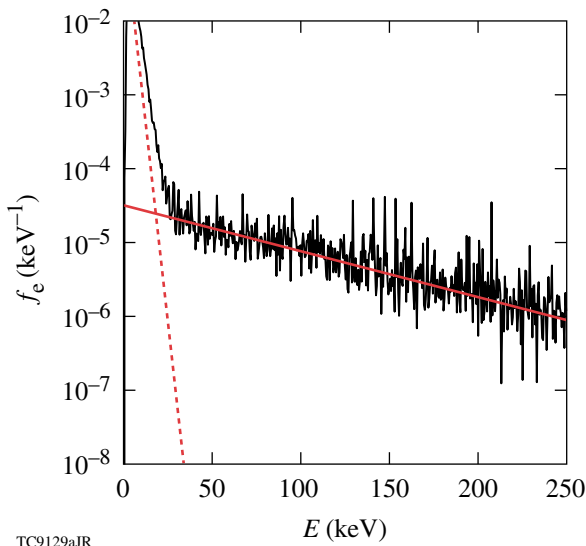

TC9129aJR

Figure 126.21
The electron test-particle distribution function $f_e(E)$ as a function of electron energy E constructed from an ensemble of 10^6 trajectories. The slope of the distribution function for energies $E \lesssim 30$ keV is close to the temperature of the sample distribution ($T_e = 2$ keV) as indicated by the steep dashed red line. For energies $E \gtrsim 30$ keV, a hot tail is observed. The slope of the hot tail is well fit by an exponential (solid red line), which is used to define an exponential slope temperature T_{hot}.

Figure 126.22 shows the hot-electron temperature T_{hot} inferred from a series of simulations, with the parameters as defined above, plotted against the threshold parameter η. Recall that density scale length and laser intensity are being varied, and while there is a small scatter in the inferred temperature for different combination of L_n and I giving the same η, the hot temperature is well predicted by the value of η alone. A hot component is generated once η has slightly exceeded unity
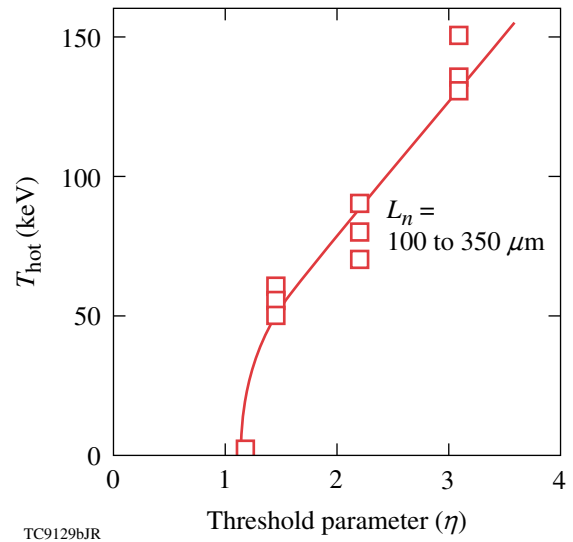
TC9129bJR

Figure 126.22
The hot-electron temperature T_{hot} as determined by the electron test-particle distribution function for a series of extended Zakharov realizations plotted against the threshold parameter $\eta[= I_{14}L_{\mu m}/(230 \text{ keV})]$. For a given η, the open squares show the effect of varying the density scale length in the range $L_n = (100 \text{ to } 350) \mu m$ while holding the initial electron temperature T_e fixed (intensities were adjusted appropriately). The red (solid) line indicates the general trend.

(which is also an experimental observation[3]) and increases from $T_{hot} \sim 50$ keV at $\eta = 2$ to a value of ~140 keV at $\eta = 3.0$.

The insensitivity of the hot-electron temperature to density scale length for a fixed value of the threshold parameter η is shown in Fig. 126.23. Once again, as the density scale length is increased, the laser intensity is decreased in order to keep the value of η constant. Solid lines connect simulation points having constant η, while the filled markers correspond to a laser intensity of $I_L = 4.8 \times 10^{14}$ W/cm^2. From the filled markers, the rapid increase in hot-electron temperature with density scale length can be visualized. The reason for this insensitivity can be determined upon an examination of the Zakharov predictions for the nonlinearly saturated LW spectrum in each case. Figure 126.24 shows the rms electric field taken over each Zakharov simulation volume (adjusted with L_n to span the density range of $0.19 < n_e/n_c < 0.27$). While the value of $\langle E \rangle_{rms}$ depends on the value of the threshold parameter for a given scale length and is of the order of $\langle E \rangle_{rms} = 10^6$ statvolts/cm for fixed η, it decreases with density scale length. It is therefore the laser intensity that determines the level of LW excitation. The acceleration of hot electrons, very crudely speaking, is given by the characteristic electric field multiplied by the acceleration length. In this way, the increasing acceleration length is offset by the reduction in electric field.

The above results have ignored the possibility of multiple transits of the hot electrons through the quarter-critical region
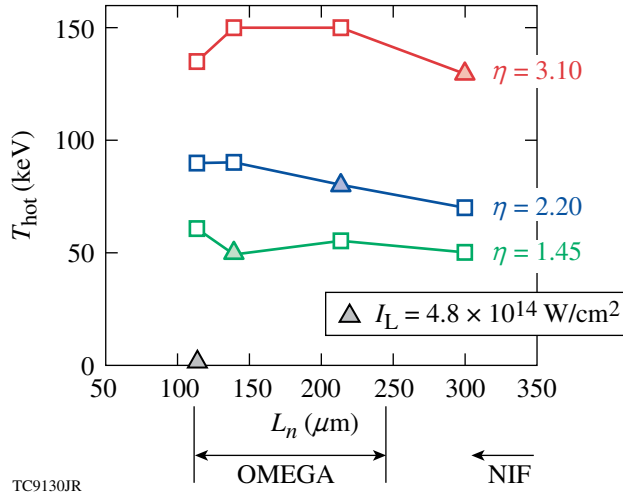

Figure 126.23

The hot-electron temperature T_{hot} in keV as determined by the electron test-particle distribution function for a series of extended Zakharov realizations plotted against density scale length L_n in microns. The upper (red), middle (blue), and lower (green) curves correspond to values of the threshold parameter of $\eta = 3.10$, 2.20, and 1.45, respectively. The filled triangles correspond to a laser intensity of $I_L = 4.8 \times 10^{14}$ W/cm^2. In all cases the initial electron temperature was $T_e = 2.0$ keV.
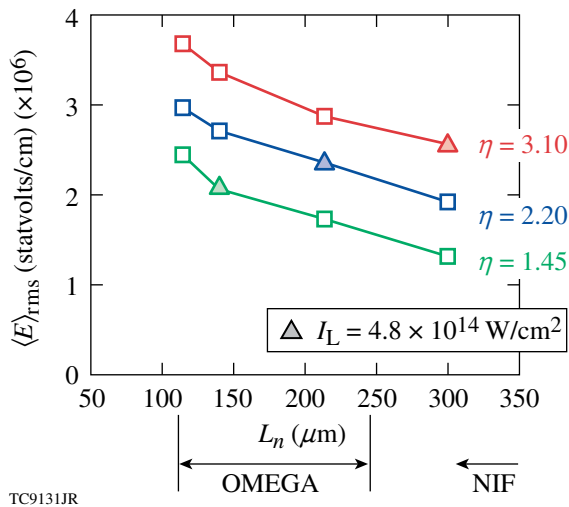

Figure 126.24

The root-mean-square electric field at saturation obtained from a series of extended Zakharov runs with an electron temperature $T_e = 2$ keV plotted against density scale length L_n in microns. The upper (red), middle (blue), and lower (green) curves correspond to values of the threshold parameter of $\eta = 3.10$, 2.20, and 1.45, respectively. It is evident that for a given value of η and for a fixed electron temperature, the rms electric field decreases with an increase (decrease) in density scale length L_n (laser intensity I_L). The filled markers correspond to a laser intensity of $I_L = 4.8 \times 10^{14}$ W/cm^2.

and therefore multiple stages of acceleration. The size of this effect has been demonstrated by implementing the boundary conditions exactly as described in **Practical Implementation of Delay-Type Boundary Conditions on Test Particles** (p. 74) (see Fig. 126.25). Look-up tables corresponding to shot 45009 at a time near the peak drive, when $\rho R \approx 1 \times 10^{-2}$ g/cm^2, have been used (Figs. 126.19 and 126.20). In Fig. 126.25 the square symbols show the hot-electron temperature as a function of the threshold parameter η with absorbing boundaries, while the circles show the hot-electron temperature when the "physical" boundary conditions are adopted. It can be seen that there is a significant effect; corresponding to an (~3×) increase in the hot-electron temperature. This demonstrates the futility of studying an isolated region of the target near the quarter-critical density when attempting to compute hot-electron temperature and, by extension, the expected hot-electron preheat. This is an extremely unfortunate result since the mixing of spatial scales is severe. On one hand, the LW wavelength must be resolved (which is submicron), while on the other, electron trajectories must be traced over millimeters. A similar mixing (four orders of magnitude) also holds for the temporal scale.

The size of the effect obviously increases in importance with higher one-pass temperatures since more-energetic electrons can more freely pass through the core. So as to not overstate
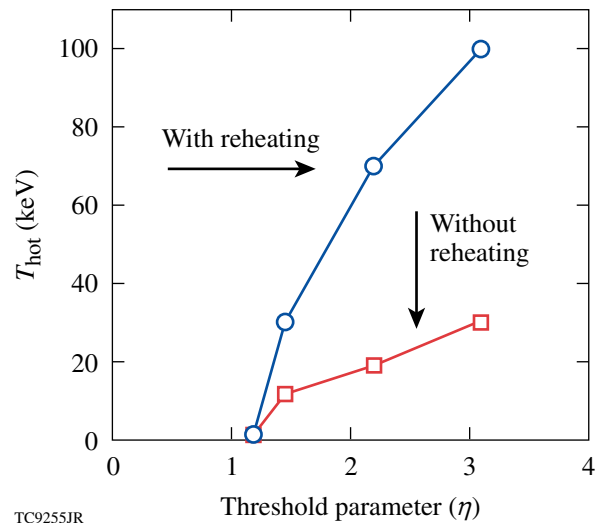

Figure 126.25

The hot-electron temperature T_{hot} in keV as a function of the threshold parameter η. The hot temperature was determined from the electron test-particle energy distribution for test-particle trajectories employing thermal boundary conditions (red curve) and delay-type boundary conditions as described on p. 74 (blue curve). The density scale length L_n and electron temperature T_e were held constant at 150 μm and 2 keV, respectively, while the intensity was varied.

the size of the effect, the one-pass temperatures were actually reduced from the pure Zakharov predictions in making these calculations (e.g., comparison of Fig. 126.25 with Fig. 126.22 shows a smaller one-pass temperature). In fact, when computing test-particle heating for Fig. 126.25, the predicted electric field $\vec{E}$ has been reduced artificially ("renormalized") in magnitude [only where it appears in Eq. (6)] so that the resulting hot-electron temperature, in the case of thermal boundaries, is computed to be no larger than the best current estimate based on reduced description particle-in-cell modeling.[28] It might be expected that the non-self-consistent test particle model would lead to exaggerated hot-electron temperatures because of the absence of any modification to the linear dispersion (damping) caused by the hot tail. It is hoped that a self-consistent treatment using a quasilinear model will remove the need for such renormalization.

Summary and Discussion

An extended Zakharov model of two-plasmon-decay instability has been presented and used to predict the saturated LW spectrum in the absence of electron kinetic effects (heating). The parameters were motivated by current OMEGA experiments, and the assumed electron temperature and density profiles were defined by 1-D radiation hydrodynamic (*LILAC*) calculations for a given time corresponding to peak TPD instability.

The LW spectrum has been observed to evolve as a consequence of the interaction between the unstable LW's and LF density fluctuations. It was argued that convectively unstable modes come to dominate the late-time spectrum, while the absolute TPD model is relatively unimportant after initial saturation by profile modification. The convective modes are either linearly saturated close to threshold or by ponderomotively driven ion-acoustic turbulence once threshold is exceeded significantly. It was noted that several tens of picoseconds are required for the LW spectrum to approach a statistical steady state.

Hot-electron production was first calculated by a non-self-consistent test particle approach using the Zakharov predictions for the electric fields at saturation and with the assumption of thermal boundary conditions. An exponential hot-electron tail was observed once the absolute threshold was exceeded ($\eta > 1$), and the characteristic temperature of this tail increased from approximately $T_{hot} = 50$ keV for $\eta \approx 1.5$ to a value of $T_{hot} = 140$ keV when $\eta = 3$. These temperatures were shown to be reasonable based on estimates of the maximum-allowable energy gain over the interaction region, and they are also broadly consistent with experimental measurements and RPIC simulations.

It was noted that electron heating also depends on the global details of the implosion because of the long-range nature of the hot electrons and the possibility of reheating [as has been described in **Practical Implementation of Delay-Type Boundary Conditions on Test Particles** (p. 74)]. This effect has been captured by using a particular form of boundary condition on the test-particle trajectories. A prescription for such boundary conditions has been constructed and described. Adoption of these boundary conditions was shown to lead to an increase in the computed hot-electron temperature by a factor of ~3×. It was noted that any attempt to model the hot-electron temperature or preheat in such targets must account for this physical effect.

The model allows for systematic refinement. Future plans in this regard include the inclusion of a propagating scattered transverse EM envelope at a frequency $\omega_0/2$ so that absolute Raman and high-frequency hybrid instability[18] may be included. The test-particle method developed here, together with reduced particle-in-cell calculations,[10] will be used to guide the development of a self-consistent quasilinear model of electron heating. This will require the inclusion of the delay-type boundary conditions and an investigation into the effects of density inhomogeneity. The delay-type boundary condition model can also be improved. In particular, a self-consistent model for the sheath potential will be developed, and the effect of angular scattering will also be taken into account when computing electron trajectories.

Finally, diagnostics such as preheat, half-harmonic emission, and bremsstrahlung spectra[26,48] will be added to the model to facilitate comparison with experiment.

REFERENCES

1. J. D. Lindl *et al.*, Phys. Plasmas **11**, 339 (2004).

2. S. P. Regan, N. B. Meezan, L. J. Suter, D. J. Strozzi, W. L. Kruer, D. Meeker, S. H. Glenzer, W. Seka, C. Stoeckl, V. Yu. Glebov, T. C. Sangster, D. D. Meyerhofer, R. L. McCrory, E. A. Williams, O. S. Jones, D. A. Callahan, M. D. Rosen, O. L. Landen, C. Sorce, and B. J. MacGowan, Phys. Plasmas **17**, 020703 (2010).

3. W. Seka, D. H. Edgell, J. F. Myatt, A. V. Maximov, R. W. Short, V. N. Goncharov, and H. A. Baldis, Phys. Plasmas **16**, 052701 (2009).

4. C. Stoeckl, R. E. Bahr, B. Yaakobi, W. Seka, S. P. Regan, R. S. Craxton, J. A. Delettrez, R. W. Short, J. Myatt, A. V. Maximov, and H. Baldis, Phys. Rev. Lett. **90**, 235002 (2003).

5. J. A. Delettrez, V. N. Goncharov, P. B. Radha, C. Stoeckl, A. V. Maximov, T. C. Sangster, J. A. Frenje, and D. Shvarts, Bull. Am. Phys. Soc. **52**, 143 (2007).

6. D. Shvarts, V. A. Smalyuk, R. Betti, J. A. Delettrez, D. H. Edgell, V. Yu. Glebov, V. N. Goncharov, R. L. McCrory, P. W. McKenty, D. D. Meyerhofer, F. J. Marshall, P. B. Radha, T. C. Sangster, W. Seka, S. Skupsky, C. Stoeckl, B. Yaakobi, J. A. Frenje, C. K. Li, R. D. Petrasso, and F. H. Séguin, presented at the 37th Anomalous Absorption Conference, Maui, HI, 27–31 August 2007.

7. V. A. Smalyuk, D. Shvarts, R. Betti, J. A. Delettrez, D. H. Edgell, V. Yu. Glebov, S. X. Hu, F. J. Marshall, R. L. McCrory, P. W. McKenty, D. D. Meyerhofer, P. B. Radha, T. C. Sangster, W. Seka, S. Skupsky, C. Stoeckl, B. Yaakobi, J. A. Frenje, C. K. Li, R. D. Petrasso, and F. H. Séguin, presented at the 37th Anomalous Absorption Conference, Maui, HI, 27–31 August 2007.

8. V. N. Goncharov, T. C. Sangster, P. B. Radha, R. Betti, T. R. Boehly, T. J. B. Collins, R. S. Craxton, J. A. Delettrez, R. Epstein, V. Yu. Glebov, S. X. Hu, I. V. Igumenshchev, J. P. Knauer, S. J. Loucks, J. A. Marozas, F. J. Marshall, R. L. McCrory, P. W. McKenty, D. D. Meyerhofer, S. P. Regan, W. Seka, S. Skupsky, V. A. Smalyuk, J. M. Soures, C. Stoeckl, D. Shvarts, J. A. Frenje, R. D. Petrasso, C. K. Li, F. Séguin, W. Manheimer, and D. G. Colombant, Phys. Plasmas **15**, 056310 (2008).

9. R. Yan, A. V. Maximov, C. Ren, and F. S. Tsung, Phys. Rev. Lett. **103**, 175002 (2009).

10. H. X. Vu, D. F. DuBois, D. A. Russell, and J. F. Myatt, Phys. Plasmas **17**, 072701 (2010).

11. D. A. Russell, presented at the Workshop on Laser Plasma Instabilities, sponsored by Lawrence Livermore National Laboratory and the University of Rochester's Laboratory for Laser Energetics, Livermore, CA, 3–5 April 2002.

12. Y. C. Lee and P. K. Kaw, Phys. Rev. Lett. **32**, 135 (1974).

13. A. Simon, R. W. Short, E. A. Williams, and T. Dewandre, Phys. Fluids **26**, 3107 (1983).

14. L. V. Powers and R. L. Berger, Phys. Fluids **27**, 242 (1984).

15. L. V. Powers and R. L. Berger, Phys. Fluids **28**, 2419 (1985).

16. L. V. Powers and R. L. Berger, Plasma Phys. Control. Fusion **28**, 1575 (1986).

17. B. K. Sinha and G. P. Gupta, Plasma Phys. Control. Fusion **35**, 281 (1993).

18. B. B. Afeyan and E. A. Williams, Phys. Rev. Lett. **75**, 4218 (1995).

19. B. B. Afeyan and E. A. Williams, Phys. Plasmas **4**, 3845 (1997).

20. A. C. Machacek and J. S. Wark, Phys. Plasmas **8**, 4357 (2001).

21. A. C. Machacek and J. S. Wark, Phys. Plasmas **8**, 704 (2001).

22. R. Yan, A. V. Maximov, and C. Ren, Phys. Plasmas **17**, 052701 (2010).

23. M. N. Rosenbluth, Phys. Rev. Lett. **29**, 565 (1972).

24. J. F. Drake and Y. C. Lee, Phys. Rev. Lett. **31**, 1197 (1973).

25. D. A. Russell and D. F. DuBois, Phys. Rev. Lett. **86**, 428 (2001).

26. D. F. DuBois, D. A. Russell, and H. A. Rose, Phys. Rev. Lett. **74**, 3983 (1995).

27. J. Delettrez, R. Epstein, M. C. Richardson, P. A. Jaanimagi, and B. L. Henke, Phys. Rev. A **36**, 3926 (1987).

28. D. F. DuBois and H. X. Vu, Los Alamos National Laboratory and University of California—San Diego, private communication (2010).

29. K. Y. Sanbonmatsu *et al.*, Phys. Rev. Lett. **82**, 932 (1999).

30. K. Y. Sanbonmatsu *et al.*, Phys. Plasmas **7**, 2824 (2000).

31. J. J. Thomson, R. J. Faehl, and W. L. Kruer, Phys. Rev. Lett. **31**, 918 (1973).

32. J. I. Katz *et al.*, Phys. Fluids **16**, 1519 (1973).

33. K. Y. Sanbonmatsu *et al.*, Geophys. Res. Lett. **24**, 807 (1997).

34. A. B. Langdon, B. F. Lasinski, and W. L. Kruer, Phys. Rev. Lett. **43**, 133 (1979).

35. C. Ren, University of Rochester, private communication (2010).

36. H. A. Baldis and C. J. Walsh, Phys. Fluids **26**, 1364 (1983).

37. R. W. Short, Bull. Am. Phys. Soc. **55**, 115 (2010).

38. H. X. Vu, D. F. DuBois, J. F. Myatt, and D. A. Russell, "Langmuir Waves Collapse and Associated Suprathermal Electron Production by the Two-Plasmon Decay Instability in Inhomogeneous Plasmas," submitted to Physical Review Letters.

39. W. L. Kruer, *The Physics of Laser–Plasma Interactions, Frontiers in Physics*, Vol. 73, edited by D. Pines (Addison-Wesley, Redwood City, CA, 1988).

40. Y. Elskens and D. Escande, *Microscopic Dynamics of Plasmas and Chaos*, Series in Plasma Physics (Institute of Physics Publishing, Bristol, England, 2003).

41. W. Rozmus and P. P. Goldstein, Phys. Rev. A **38**, 5745 (1988).

42. R. D. Brooks and Z. A. Pietrzyk, Phys. Fluids **30**, 3600 (1987).

43. D. Pesme, Phys. Scr. **T50**, 7 (1994).

44. J. J. Thomson *et al.*, Phys. Fluids **17**, 973 (1974).

45. H. O. Wyckoff, *ICRU Report*, International Commission on Radiation Units and Measurements, Inc., Bethesda, MD (1984).

46. J. S. Pearlman and G. H. Dahlbacka, Appl. Phys. Lett. **31**, 414 (1977).

47. D. M. Villeneuve, R. L. Keck, B. B. Afeyan, W. Seka, and E. A. Williams, Phys. Fluids **27**, 721 (1984).

48. J. Meyer and Y. Zhu, Phys. Rev. Lett. **71**, 2915 (1993).